Materials Advances

ROYAL SOCIETY OF CHEMISTRY

PAPER

View Article Online
View Journal | View Issue

Cite this: *Mater. Adv.*, 2024, 5, 3965

The introduction of gallium ions into V_2O_5 interlayers for highly reversible Zn ion batteries

Ming Zhao,[a] Shilong Li,[a] Xiang Wu *[a] and Abdukayum Abdukader *[b]

Received 26th November 2023,
Accepted 17th March 2024

DOI: 10.1039/d3ma01052j

rsc.li/materials-advances

It is very important to construct energy storage systems with high safety and excellent electrochemical performance. In particular, aqueous Zn ion batteries (AZIBs) possess the characteristics of low-cost and environmental benignity. However, there are few cathode materials that match well with the zinc anode. Herein, Ga^{3+} pre-intercalation into V_2O_5 layers promotes the insertion/extraction kinetics of zinc ions. The assembled Zn/V_2O_5–0.1Ga battery with 3 M $Zn(CF_3SO_3)_2$ electrolyte shows a specific capacity of 512.07 mA h g^{-1} at a current density of 0.1 A g^{-1}. It delivers an energy density of 281.64 W h kg^{-1} at a power density of 55 W kg^{-1}. It can also provide a reversible capacity of 110 mA h g^{-1} at 10 A g^{-1} with a retention rate of 91.43% after 5000 cycles, revealing its potential applications in future energy storage devices.

1. Introduction

In the past few years, the excessive depletion of fossil fuels has caused a serious energy crisis and environmental pollution. It is necessary to design and develop many sustainable energy sources.[1–4] Among them, Li-ion batteries (LIBs) have been utilized in smartphones, electric vehicles and laptops. Nevertheless, their future development is still restricted considering the high cost and toxic organic electrolyte.[5,6] Thus, it is crucial to seek an alternative to LIBs, such as rechargeable aqueous multivalent ion batteries (Na, K, Ca, Zn, and Mg).[7–10] Aqueous zinc ion batteries (AZIBs) attract wide attention owing to their high theoretical capacity (820 mA h g^{-1}), and the abundant resources and low redox potential of Zn^{2+}/Zn (−0.76 V *vs.* SHE).[11–13] However, it is still an urgent task to explore suitable cathode materials, such as Prussian blue analogues, and Mn-based and vanadium-based materials.[14,15] Prussian blue analogues show low capacity and short cycle life.[16] Manganese-based materials still need to be improved owing to low rate performance and unstable structures.[17,18]

Recently, various V_2O_5 structures have been widely investigated as cathode materials for AZIBs,[19] owing to their diverse oxidation states (V^{2+}, V^{3+}, V^{4+}, and V^{5+}) and unique crystal features.[20,21] The crystal structure of V_2O_5 connects the distorted VO_5 square cones through the shared edges and corners to form a 2D layered structure with weak van der Waals interactions between the layers. For instance, Chen *et al.* prepared V_2O_5 samples supported on carbon cloth by a template route. The fabricated cells delivered a capacity of 370 mA h g^{-1} at 0.2 A g^{-1}.[22] The Zn/V_2O_5@CNT devices presented a capacity of 485.8 at 0.1 A g^{-1}.[23] However, the capacity of the reported V_2O_5 electrode materials is far from their theoretical capacity (589 mA h g^{-1}). The strong electrostatic repulsion between the zinc ions and the host structure results in a slow electrochemical kinetic behavior. Therefore, some strategies have been proposed to modify the cathode material of AZIBs, such as metal ion pre-embedding, defect engineering and coating of other materials.

Metal ion pre-embedding is thought to be an efficient strategy to enhance the electrochemical performance of AZIBs. Many metal cations have been introduced into target materials, such as Zn, K, and Ca. Zhang *et al.* introduced La^{3+} into a layered V_2O_5 structure. The assembled device shows a capacity of 405 mA h g^{-1} at 0.1 A g^{-1} and energy density of 227.5 W h kg^{-1} at 55 W kg^{-1}.[24] The Zn/V_2O_5 cells deliver a discharge capacity of 350 mA h g^{-1} at 0.1 A g^{-1} by the intercalation of PANI.[25] Liu and coworkers used K^+ ions as a structure pillar for introduction into V_2O_5 interlayers. The resulting material possessed a capacity of 479.8 mA h g^{-1} at 0.2 A g^{-1} and maintained 91.3% of its initial capacity at 10 A g^{-1} after 3000 cycles.[26]

In this work, we prepare Ga^{3+}-intercalated V_2O_5 nanobelts by a simple hydrothermal route. Gallium possesses natural advantages, such as its strong electronegativity forming stable chemical bonds. It has a small radius compared to other cations, making it easier to approach the target sample. The introduction of metal ions promotes the transfer of Zn ions, and maintains structural stability of the electrode materials. A series of zinc ion batteries are assembled using the obtained

[a] *School of Materials Science and Engineering, Shenyang University of Technology, Shenyang 110870, P. R. China. E-mail: wuxiang05@sut.edu.cn*
[b] *Xinjiang Key Laboratory of Novel Functional Materials Chemistry, College of Chemistry and Environmental Sciences, Kashi University, Kashi 844000, P. R. China. E-mail: abdukadera@sina.com*

V_2O_5–0.1Ga samples as cathodes. The cells deliver a discharge capacity of 512.07 mA h g^{-1} at 0.1 A g^{-1}. They maintain 91.43% of the original capacity at 10 A g^{-1} after 5000 cycles. The batteries present an energy density of 281.64 W h kg^{-1} at a power density of 55 W kg^{-1}. This work provides new ideas in designing cathode materials that match well with Zn anodes.

2. Experimental section

All the purchased chemicals were used without any purification. Typically, 4 mmol V_2O_5 (Alfa Aesar) powder was dissolved into 50 mL of de-ionized water and stirred for 30 min at 50 °C. Then, 1 mL of 30% H_2O_2 was added into the above solution. After that, a certain amount of HCl (Codow) solution is uniformly dispersed into the above mixture to adjust the pH to 1. Subsequently, 0.1 mmol $Ga(NO_3)_3{\cdot}xH_2O$ (Macklin) was added into the prepared solution with stirring for half an hour. Then, the solution was placed into an 80 mL Teflon-lined stainless-steel autoclave and maintained at 180 °C for 48 h. After cooling to room temperature, the solution was washed with alcohol and deionized water several times and dried under vacuum at 60 °C for 12 h. For comparison, different amounts of $Ga(NO_3)_3{\cdot}xH_2O$ (0, 0.05, and 0.2 mmol) were also added to similar solutions and the prepared samples were labeled as V_2O_5, V_2O_5–0.05Ga, and V_2O_5–0.2Ga, respectively.

2.1. Structural characterization

The crystallographic information of the as-prepared samples was characterized by powder X-ray diffraction (XRD, 7000, Shimadzu, Cu Kα radiation, λ = 0.1541 nm, 40 kV), scanning electron microscopy (SEM, Gemini 300-71-31), and X-ray photoelectron spectroscopy (XPS, Thermo Kalpha). The specific surface area was studied by the Brunauer–Emmett–Teller (BET, Micromeritics ASAP, JW-TB200) method.

2.2. Electrochemical measurements

The cathode materials consist of the active materials, carbon black (Power Origin Limited) and polyvinylidene fluoride (Power Origin Limited) with a mass ratio of 7 : 2 : 1. Then a certain amount of *N*-methyl-L-2-pyrrolidone (Damao) was added to form a slurry, which was evenly pressed onto graphite paper. A piece of zinc foil was used as the anode with a thickness of 0.2 mm. The coin cells (CR2032) were assembled by using 3 M $Zn(CF_3SO_3)_2$ (Bidepharm) as the electrolyte. The average loading mass of the cathode is about 1.5 mg. The galvanostatic intermittent titration technique (GITT), galvanic charge–discharge (GCD) analysis and cycling stability tests were performed at a voltage range of 0.4–1.5 V using a Neware battery tester (CT-4008T-5V6A-164). The CV curves and Nyquist plots of the cells were measured by using an electrochemical workstation (Shanghai Chenhua, CHI660E).

3. Results and discussion

First, the crystal structures of the samples are investigated by XRD, as shown in Fig. 1a. It can be observed that the diffraction peaks match well with the V_2O_5 phase (PDF# 41-1426). The V_2O_5–0.1Ga sample presents sharp and strong diffraction peaks. The main peaks at 15.30, 20.32, 21.68, 26.16, 31.04, and 41.36° belong to the (200), (001), (101), (110), (301) and

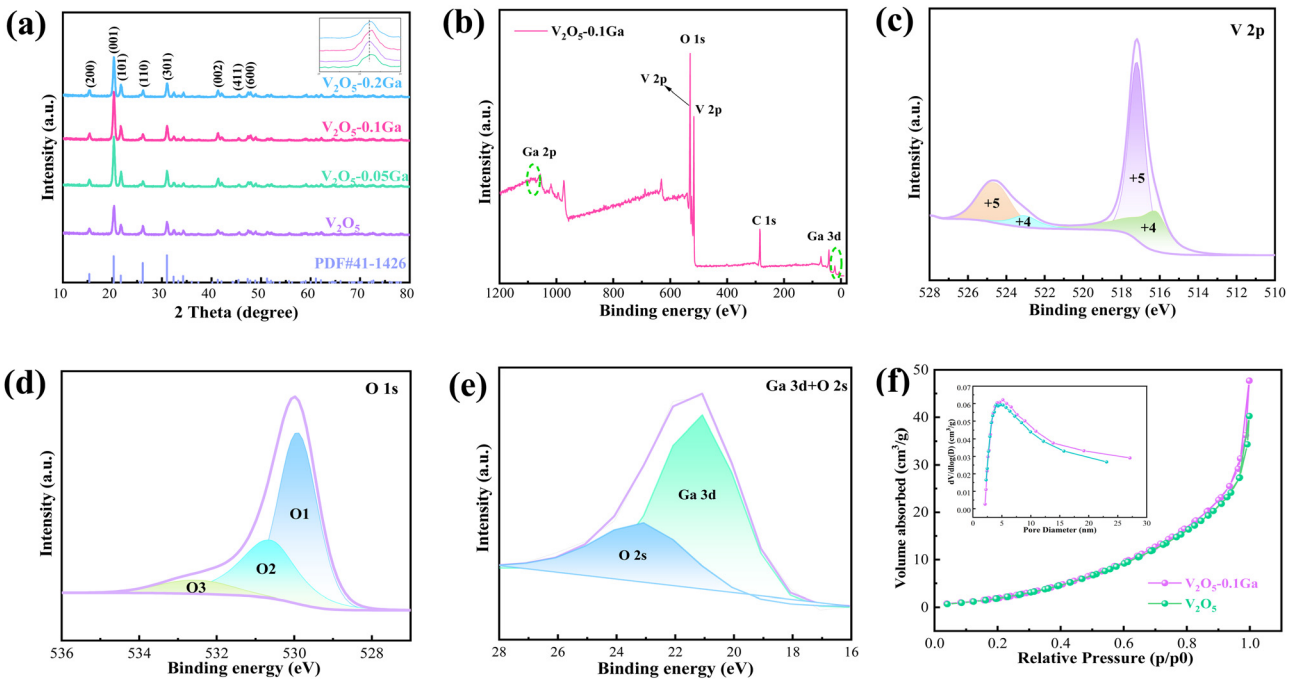

Fig. 1 Structural characterizations of the samples. (a) XRD patterns. (b) XPS survey spectrum. (c) V 2p, (d) O 1s, and (e) Ga 3d+O 2s. (f) N_2 adsorption–desorption isotherms; inset represents the pore size distributions of the V_2O_5–0.1Ga products.

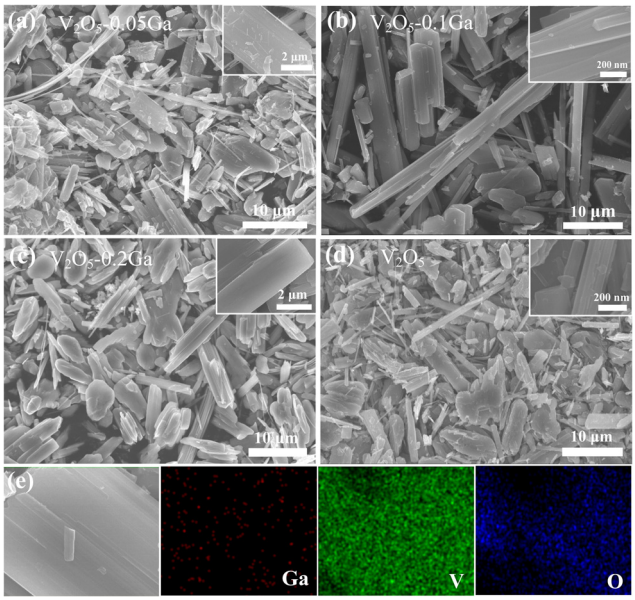

Fig. 2 SEM images of (a) V_2O_5–0.05Ga, (b) V_2O_5–0.1Ga, (c) V_2O_5–0.2Ga and (d) V_2O_5 samples. (e) The corresponding elemental mapping of the V_2O_5–0.1Ga samples.

(002) crystal planes, respectively. By enlarging the XRD pattern, it can be observed that the (101) crystal plane shifts to the right. This demonstrates the successful doping of Ga ions into the V_2O_5 host structure. The lattice parameters a = 11.516 Å, b = 3.566 Å, and c = 4.373 Å. Then XPS is used to investigate the valence states and elemental composition of the electrode materials. Fig. 1b presents the full spectrum of the V_2O_5–0.1Ga sample, revealing the existence of the V, O, Ga and C elements. From Fig. 1c, the binding energies at 516.28/523.08 eV and 517.18/524.78 eV are in accordance with V^{4+} and V^{5+}.[27] According to previous reports, V_2O_5 samples with mixed valences (V^{4+} and V^{5+}) possess fast reaction kinetics and low polarization intensity.[28] The O 1s spectrum can be fitted into three peaks, as shown in Fig. 1d. The peaks at 529.98, 530.68 and 532.68 eV can be indexed to oxygens in the metal oxide,[29] V=O bonds,[30] and O–H from surface-absorbed water,[31] respectively. The Ga 3d spectrum in Fig. 1e shows the signal peak at 20.8 eV, which confirms the presence of Ga^{3+} in the V_2O_5 samples.[32] Fig. 1f shows nitrogen adsorption and desorption isotherms of the V_2O_5 and V_2O_5–0.1Ga samples. The specific surface area of V_2O_5–0.1Ga is 27.42 $m^2\ g^{-1}$, which is larger than that of the V_2O_5 product (24.09 $m^2\ g^{-1}$). In addition, the total pore volumes of the V_2O_5–0.1Ga and V_2O_5 samples are 0.061 and 0.052 $cm^3\ g^{-1}$, respectively. The results demonstrate that the addition of Ga element can increase the specific surface area and the active sites.

SEM is then utilized to observe the morphologies of the samples. As described in Fig. 2a–d, the growth process of the V_2O_5 samples is investigated by controlling the content of Ga^{3+}. In Fig. 2b, the V_2O_5–0.1Ga electrode possesses a belt-like shape. In contrast, the other three samples show uneven microcrystals. Using V_2O_5–0.1Ga samples as a cathode, the exposed surface is expected to provide abundant active sites to obtain superior rate performance. As seen in Fig. 2e, the elemental mapping confirms a uniform distribution of three elements of V, O and Ga along the surface of the nanobelts, which demonstrates that Ga^{3+} is doped into the V_2O_5 host structure.

To study the electrochemical performance of the samples, some CR2032 coin cells are assembled with 3 M $Zn(CF_3SO_3)_2$ as the electrolyte. Fig. 3a shows the first five cycle CV curves of the

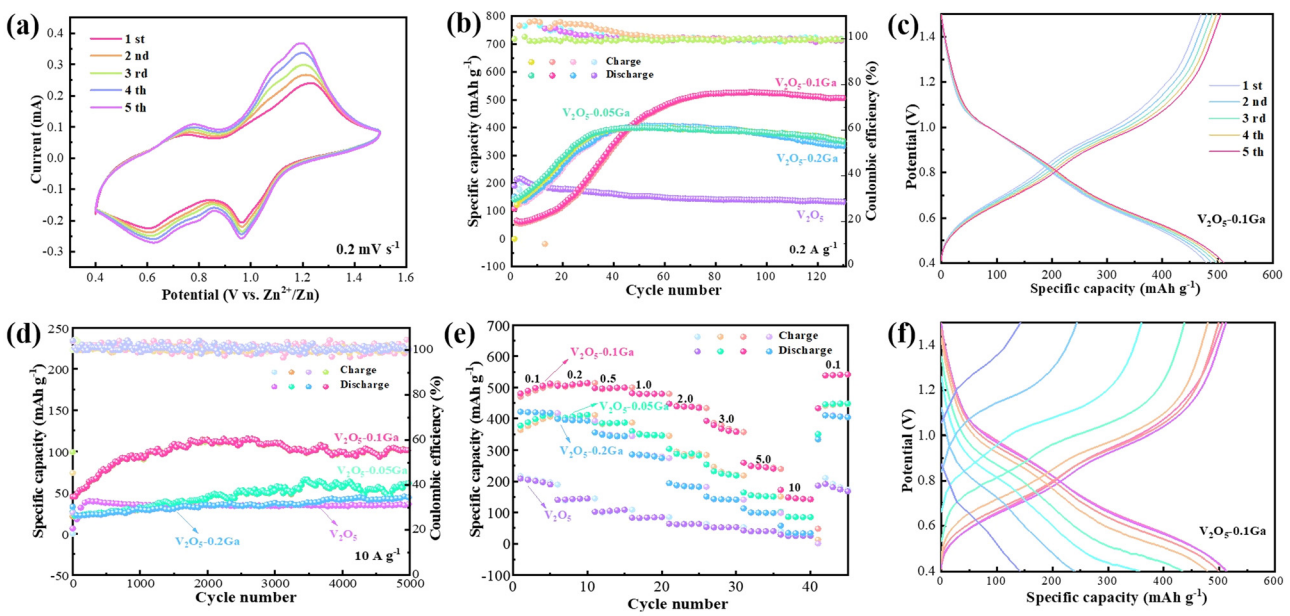

Fig. 3 Electrochemical performance. (a) CV curves in the first 5 cycles at 0.2 mV s^{-1}, (b) cycling performance at 0.2 A g^{-1}, (c) GCD curves of the first five cycles at 0.1 A g^{-1}, (d) long-term cycling at 10 A g^{-1}, (e) rate capability at different current densities and (f) GCD curves at various current densities.

Table 1 The electrochemical performance of the V_2O_5–0.1Ga electrode materials

Materials	Morphology	Current density (A g^{-1})	Discharge capacity (mA h g^{-1})	Electrolyte	Ref.
VO_2@PPy	Hollow spheres	0.1	440	3 M $Zn(CF_3SO_3)_2$	33
V_2O_5	Nanofibers	0.02	319	3 M $Zn(CF_3SO_3)_2$	34
Mn-doped-VO_2	Nanobelts	0.1	209.6	3 M $Zn(CF_3SO_3)_2$	35
$Ni_{0.25}V_2O_5{\cdot}nH_2O$	Nanoribbons	0.2	389	3 M $ZnSO_4$	36
$VO_2{\cdot}0.2H_2O$	Nanocuboids	0.25	423	2 M $ZnSO_4$	37
V_2O_{5x}/PANI	Nanosheets	0.1	400	2 M $ZnSO_4$	38
$K_{1.15}V_5O_{13}{\cdot}1.3H_2O$	Nanobelts	0.2	461	3 M $Zn(OTF)_2$	39
$Ba_{1.2}V_6O_{16}{\cdot}3H_2O$	Nanobelts	0.1	321	2 M $ZnSO_4$	40
V_2O_5	Hollow spheres	0.2	280	3.65 M $ZnSO_4$	41
V_2O_5–0.1Ga	Nanobelts	0.1	512.07	3 M $Zn(CF_3SO_3)_2$	This work

V_2O_5–0.1Ga sample at 0.2 mV s^{-1}. The curves maintain the same shapes well, indicating their high reversibility of the redox reactions. Furthermore, there are two pairs of redox peaks located at 1.19/0.96 V and 0.77/0.62 V, which are related to the multi-step intercalation/de-intercalation of Zn^{2+}. Fig. 3b presents the cycling stability of the samples. After many cycles of activation, the discharge capacity of the V_2O_5–0.1Ga sample delivers a specific capacity of 526.8 mA h g^{-1} at 0.2 A g^{-1} and maintains a retention rate of 95.8% after 130 cycles. The GCD curves of the V_2O_5–0.1Ga products show several charge–discharge platforms (Fig. 3c), which are in accordance with the corresponding CV curves shown in Fig. 3a.

The cycling stability of the cells is also evaluated at 10 A g^{-1}, as depicted in Fig. 3d. The capacity of the V_2O_5–0.1Ga sample reaches 110 mA h g^{-1} with a retention rate of 91.43% after 5000 cycles. Fig. 3e shows the corresponding rate performance of the batteries. The discharge specific capacities of the V_2O_5–0.1Ga electrodes are 512.07, 514.03, 499.67, 479.18, 437.59, 360.66, 244.64, are 148.40 mA h g^{-1} at current densities from 0.1 to 10 A g^{-1}. When it returns to 0.1 A g^{-1}, the battery still obtains a capacity of 540.57 mA h g^{-1}. This demonstrates that the moderate amount of Ga^{3+} is conducive to the enhancement of the specific capacity and rate capability. On the contrary, excessive Ga^{3+} incorporation may lead to the disruption of the crystal structure and volume expansion of the V_2O_5 samples, thus producing adverse effects. Furthermore, the GCD curves (Fig. 3f) of the Zn/V_2O_5–0.1Ga batteries show that the capacity decreases with increasing current density. Table 1 lists the zinc-ion storage performance of several electrode materials.[33–41] It demonstrates the excellent electrochemical performance of Zn/V_2O_5–0.1Ga cells.

Fig. 4a presents the CV curves of the Zn/V_2O_5–0.1Ga cells at various scan rates (0.2–1.0 mV s^{-1}). With the increasing of the sweep speed, the positive and negative peak currents move to high and low potentials, respectively. The shape of the curves remains almost unchanged, showing their excellent reversibility. For the CV curves, the relationship between peak current (i) and sweep speed (v) can be obtained through the equation as follows:

$$i = av^b \quad (1)$$

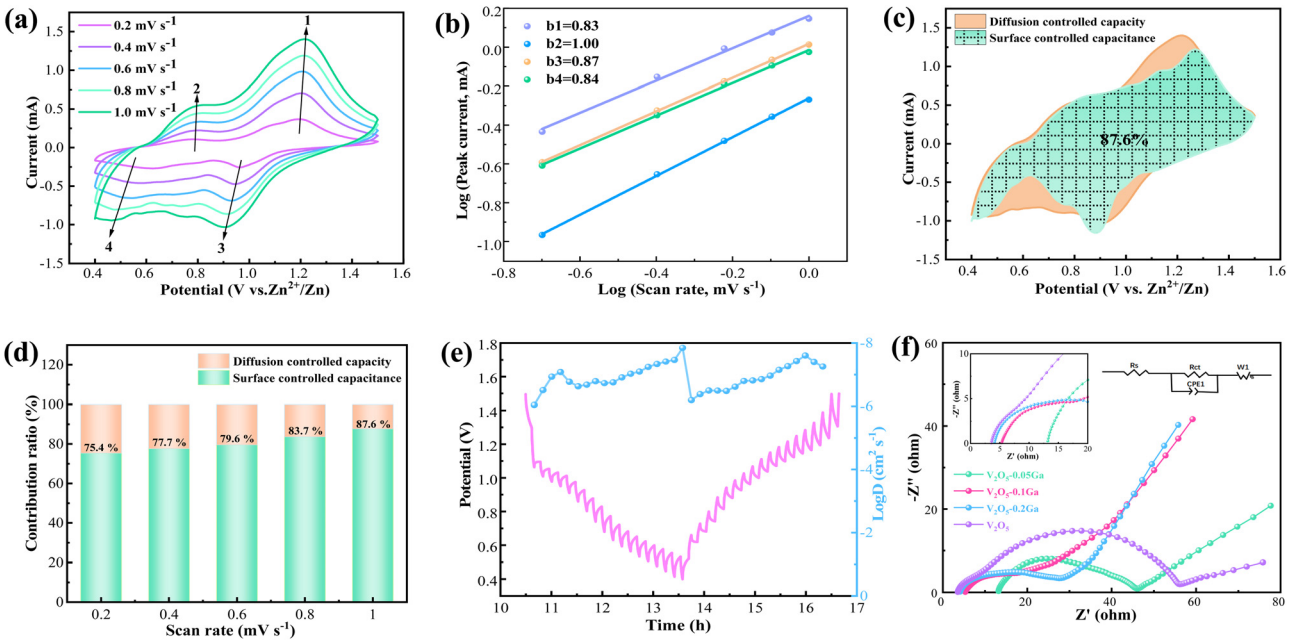

Fig. 4 Energy storage kinetics of the V_2O_5–0.1Ga electrodes for AZIBs. (a) CV curves, (b) the fitting plots of log(i) and log(v), (c) and (d) the capacitive contribution ratios at various scan rates, (e) GITT curves and (f) Nyquist plots.

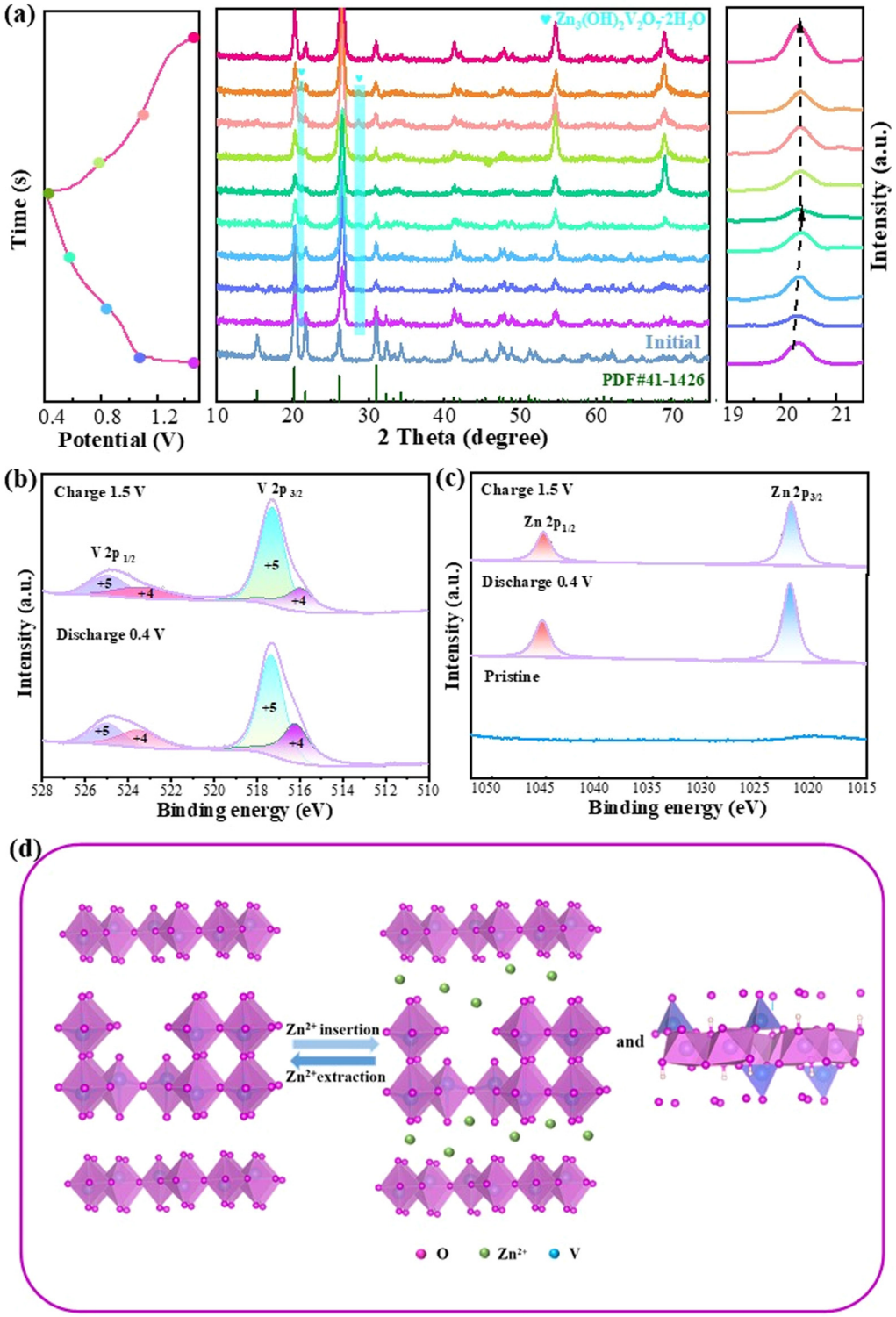

Fig. 5 Structural and morphology characterization. (a) *Ex situ* XRD patterns at various charge/discharge states, (b) and (c) XPS spectra of V and Zn elements and (d) schematic diagram of the Zn^{2+} insertion mechanism on the V_2O_5–0.1Ga cathode.

where a and b are adjustable constants. The b value can be obtained by a linear fitting. The electrochemical reaction is determined by a diffusion-controlled process when the value of b is close to 0.5, while it is capacitance-controlled behavior if $b \geq 1$. If the b value is 0.5–1, it indicates a pseudocapacitive contribution- and battery behavior-dominated reaction process. From Fig. 4b, the b values are 0.83, 1.00, 0.87 and 0.84, respectively. This confirms the capacitive contribution.

In addition, the following equation can be utilized to calculate the pseudocapacitive and diffusion contributions:

$$i(V) = k_1\nu + k_2\nu^{1/2} \quad (2)$$

where k_1 and k_2 are fixed constants. The parameter $k_1\nu$ is defined as the surface-controlled process, while $k_2\nu^{1/2}$ is the diffusion-controlled one. The capacitive process reaches 87.6% of the total capacity at 1.0 mV s^{-1} (Fig. 4c). In Fig. 4d, the capacitance contribution ratio increases from 75.4% to 87.6% with the sweep rate increasing. The GITT curves are characterized to further evaluate the diffusion ability of zinc ions. From Fig. 4e, the $D_{Zn^{2+}}$ values of the V_2O_5–0.1Ga sample are determined to be 10^{-6} and 10^{-8} cm^2 s^{-1} in the discharge state. This demonstrates that the V_2O_5–0.1Ga nanobelts accelerate the Zn^{2+} migration. EIS is utilized to further investigate the zinc ion storage process in the Zn/V_2O_5–0.1Ga battery. The curves consist of a semicircle in the high frequency region and a straight line in the low one. The radius of the semicircle represents the charge transfer resistance (R_{ct}) between the electrode and electrolyte. As presented in Fig. 4f, V_2O_5–0.1Ga samples possess a lower charge transfer resistance (R_{ct}) than the other samples, indicating their excellent reaction kinetics. In addition, the V_2O_5–0.1Ga samples show an R_s value of 5.1 Ω.

The energy density and power density can be calculated based on eqn (3) and (4):

$$E = QU/2m \quad (3)$$

$$P = iU/2m \quad (4)$$

where E (W h kg^{-1}) and P (W kg^{-1}) refer to the energy density and power density, respectively. Q (A h) represents the discharge capacity, U (V) is the operating voltage, i (A) denotes the discharge current, and m (kg) refers to the mass of active material. Therefore, it can be concluded that the cells possess an energy density of 281.64 W h kg^{-1} at a power density of 55 W kg^{-1} at 0.1 A g^{-1}.

Ex situ XRD was performed to study the Zn^{2+} storage mechanism of the Zn/V_2O_5–0.1Ga batteries at different stages (Fig. 5a). The (001) crystal plane shifts to a high angle when the voltage drops from 1.5 V to 0.4 V. This is due to the strong electrostatic adsorption between the intercalated Zn^{2+} and V_2O_5 materials, which reduces the interplanar spacing of the (001) plane.[42] After full charging, the plane returns to its original state, which is attributed to the reversible removal of Zn^{2+} in the host material. Besides, a new phase $Zn_3(OH)_2V_2O_7{\cdot}2H_2O$ appears during the reaction due to the insertion of Zn^{2+}, demonstrating that Zn^{2+} is embedded successfully into the V_2O_5–0.1Ga samples. The generation of a new phase is related to H^+ in the electrolyte. The electrochemical reaction process can be represented as below:

$$V^{5+} + 4H_2O \rightarrow VO_2(OH)^- + 6H^+ \quad (5)$$

$$Zn \rightarrow Zn^{2+} + 2e^- \quad (6)$$

$$2VO_2(OH)^- + 3Zn^{2+} + 3H_2O \rightarrow Zn_3(OH)_2V_2O_7{\cdot}2H_2O + 4H^+ \quad (7)$$

Finally, XPS spectra are again obtained to study the composition and chemical valence of the V_2O_5–0.1Ga electrode during the charge and discharge states. In Fig. 5b, the V $2p_{1/2}$ and V $2p_{3/2}$ diffraction peaks can be attributed to V^{4+} (523.68/516.28 eV) and V^{5+} (524.98/517.38 eV), respectively.[43] In the charge state, the signal of the V^{4+} peaks decreases, while that of V^{5+} increases. This is caused by reversible insertion/extraction of Zn^{2+} in the redox reactions. As seen in Fig. 5c, there are no Zn^{2+} signals detected in the pristine state. When discharged to 0.4 V, the peaks at 1022.18 eV and 1045.38 eV belong to Zn $2p_{3/2}$ and Zn $2p_{1/2}$. The peak signal is lower during charging than discharging. It is worth noting that the intensity of the Zn signal peak does not disappear completely after charging, which is due to the irreversible de-embedding of some Zn^{2+}. Fig. 5d illustrates an electrochemical reaction schematic of the reversible insertion/extraction of Zn^{2+}.

4. Conclusions

In summary, we have prepared several Ga-ion pre-embedded V_2O_5 nanobelts by a hydrothermal strategy. The obtained samples show large specific surface areas, which is beneficial to increasing the reaction active sites. The pre-embedding of Ga^{3+} effectively maintains the stability of the electrode material during repeated charging and discharging. The assembled Zn/V_2O_5–0.1Ga possesses an outstanding specific capacity and long cycle life after 5000 cycles and ultrafast Zn^{2+} diffusion capability. Moreover, they also achieve high energy density and power density. The superior performance V_2O_5–0.1Ga cathode materials show great potential for advanced and safe aqueous zinc ion batteries.

Author contributions

Ming Zhao: conceptualization, software, data curation, writing – original draft preparation, and methodology, Shilong Li: visualization, and Xiang Wu and Abdukayum Abdukader: supervision, writing – reviewing and editing.

Conflicts of interest

There are no conflicts to declare.

Acknowledgements

This project is supported by the Natural Science Foundation of China (no. 52172218) and the Tianshan Innovation Team Plan of Xinjiang Uygur Autonomous Region (2023D14002).

References

1 Y. Liu, Y. Liu and X. Wu, Defect engineering of vanadium-based electrode materials for zinc ion battery, *Chin. Chem. Lett.*, 2023, **34**, 107839.

2 S. Zhong, Y. S. Yu, Y. Yang, Y. Yao, L. F. Wang, S. N. He, Y. X. Yang, L. Liu, W. P. Sun, Y. Z. Feng, H. G. Pan, X. H. Rui and Y. Yu, Molecular engineering on solvation structure of carbonate electrolyte toward durable sodium metal battery at −40 °C, *Angew. Chem., Int. Ed.*, 2023, **62**, e2023011693.

3 N. M. Tri, S. Preston, P. Andrea, F. Michael G, H. Xiao, G. Ilja and S. Ullrich, Polymer-templated mesoporous lithium titanate microspheres for high-performance lithium batteries, *Mater. Adv.*, 2022, **3**, 362–372.

4 Q. Xia, T. Xia and X. Wu, PPy decorated α-Fe_2O_3 nanosheets as flexible supercapacitor electrode, *Rare Met.*, 2022, **41**, 1195–1201.

5 S. Stefan, L. Andreas, Z. Veronika, R. Joseph, G. Steffen, R. Daniel and F. Jurgen, Li^+/H^+ exchange of $Li_7La_3Zr_2O_{12}$ single and polycrystals investigated by quantitative LIBS depth profiling, *Mater. Adv.*, 2022, **3**, 8760–8770.

6 J. X. Chen, P. Alessandro, Y. Shinhee, C. D. Valbjorn, E. Vincenzo and P. Nini, *Mater. Adv.*, 2023, **4**, 6638–6644.

7 X. M. Xia, S. T. Xu, F. Tang, Y. Yao, L. F. Wang, L. Liu, S. N. He, Y. X. Yang, W. P. Sun, C. Xu, Y. Z. Feng, H. G. Pan, X. H. Rui and Y. Yu, A multifunctional interphase layer enabling superior sodium-metal batteries under ambient temperature and −40 °C, *Adv. Mater.*, 2023, **35**, 2209511.

8 J. J. Zhang and X. Wu, Dual-ion carrier storage through Mg^{2+} addition for high-energy and long-life zinc-ion hybrid capacitor, *Int. J. Miner., Metall. Mater.*, 2024, **31**, 179–185.

9 J. Xie and Q. C. Zhang, Recent progress in multivalent metal (Mg, Zn, Ca, and Al) and metal-ion rechargeable batteries with organic materials as promising electrodes, *Small*, 2019, **15**, 1805061.

10 X. Lv, F. Tang, Y. Yao, C. Xu, D. Chen, L. Liu, Y. Z. Feng, X. H. Rui and Y. Yu, Sodium gallium alloy layer for fast and reversible sodium deposition, *SusMat*, 2022, **2**, 699–707.

11 M. Zhao, S. L. Li and X. Wu, $(NH_4)_2V_{10}O_{25.8}H_2O$ nanowire materials for stable zinc ion storage, *Mater. Today Chem.*, 2023, **33**, 101686.

12 Y. X. Zeng, X. Y. Zhang, R. F. Qin, X. Q. Liu, P. P. Fang, D. Z. Zheng, Y. X. Tong and X. H. Lu, Dendrite-free zinc deposition induced by multifunctional CNT frameworks for stable flexible Zn-ion batteries, *Adv. Mater.*, 2019, **31**, 1903675.

13 Y. Liu, Y. Liu, X. Wu and Y. R. Cho, General carbon modiffcation avenue to construct highly stable V_2O_5 electrodes for aqueous zinc-ion batteries, *ACS Sustainable Chem. Eng.*, 2023, **11**, 13298–13305.

14 S. Q. Zhao, Y. Liu and X. Wu, Rose-shaped VS_2 nanosheets as cathode materials for rechargeable zinc ion batteries, *CrystEngComm*, 2023, **25**, 1986–1992.

15 Y. Liu and X. Wu, High durable aqueous zinc ion batteries by synergistic effect of V_6O_{13}/VO_2 electrode materials, *J. Energy Chem.*, 2023, **87**, 334–341.

16 Y. X. Zeng, X. F. Lu, S. L. Zhang, D. Y. Luan, S. Li and X. W. Lou, Construction of Co-Mn prussian blue analog hollow spheres for efficient aqueous Zn-ion batteries, *Angew. Chem., Int. Ed.*, 2021, **60**, 22189–22194.

17 K. X. Li, Y. Liu and X. Wu, Mn^{2+} Intercalation into hydrated vanadium pentoxide nanosheets for highly durable zinc ion batteries, *ACS Appl. Nano Mater.*, 2023, **6**, 12439–12446.

18 F. X. Shi, C. C. Mang, H. W. Liu and Y. F. Dong, Flexible and high-energy-density Zn/MnO_2 batteries enabled by electrochemically exfoliated graphene nanosheets, *New J. Chem.*, 2020, **44**, 653–657.

19 Y. Liu, Y. Liu, Y. Yamauchi, Z. A. Alothman, Y. V. Kaneti and X. Wu, Enhanced zinc ion storage capability of V_2O_5 electrode materials with hollow interior cavities, *Batteries Supercaps*, 2021, **4**, 1867–1873.

20 Y. Liu and X. Wu, Hydrogen and sodium ions co-intercalated vanadium dioxide electrode materials with enhanced zinc ion storage capacity, *Nano Energy*, 2021, **86**, 106124.

21 F. Wan and Z. Q. Niu, Design strategies for vanadium-based aqueous zinc-ion batteries, *Angew. Chem., Int. Ed.*, 2019, **58**, 16358–16367.

22 X. Zhang, Y. C. Tang, P. He, Z. Zhang and T. F. Chen, Edge-rich vertical graphene nanosheets templating V_2O_5 for highly durable zinc ion battery, *Carbon*, 2021, **172**, 207–213.

23 X. Wang, Y. M. Wang, J. N. Hao, Y. Liu, H. H. Xiao, Y. Ma, L. M. Chen, Y. Y. Huang and G. H. Yuan, Pseudocapacitive zinc cation intercalation with superior kinetics enabled by atomically thin V_2O_5 nanobelts for quasi-solid-state microbatteries, *Energy Storage Mater.*, 2022, **50**, 454–463.

24 D. D. Zhang, J. Cao, Y. L. Yue, T. Pakornchote, T. Bovornratanaraks, J. Han, X. Y. Zhang, J. Q. Qin and Y. H. Huang, Two birds with one stone: boosting zinc-ion insertion/extraction kinetics and suppressing vanadium dissolution of V_2O_5 via La^{3+} incorporation enable advanced zinc-ion batteries, *ACS Appl. Mater. Interface*, 2021, **13**, 38416–38424.

25 R. Li, F. Xing, T. Y. Li, H. M. Zhang, J. W. Yan, Q. Zheng and X. F. Li, Intercalated polyaniline in V_2O_5 as a unique vanadium oxide bronze cathode for highly stable aqueous zinc ion battery, *Energy Storage Mater.*, 2021, **38**, 590–598.

26 Y. Liu, Y. Liu, X. Wu and Y. R. Cho, High performance aqueous zinc battery enabled by potassium ion stabilization, *J. Colloid Interface Sci.*, 2022, **628**, 33–40.

27 G. A. Sawatzky and D. Post, X-ray photoelectron and auger spectroscopy study of some vanadium oxides, *Phys. Rev. B: Condens. Matter Mater. Phys.*, 1979, **20**, 1546–1555.

28 F. Liu, Z. X. Chen, G. Z. Fang, Z. Q. Wang, Y. S. Cai, B. Y. Tang, J. Zhou and S. Q. Liang, V_2O_5 nanospheres with mixed vanadium valences as high electrochemically active aqueous zinc-ion battery cathode, *Nano-Micro Lett.*, 2019, **11**, 25.

29 C. M. Ghimbeu, E. Raymundo-Pinero, P. Fioux, F. Beguin and C. Vix-Guterl, Vanadium nitride/carbon nanotube nanocomposites as electrodes for supercapacitors, *J. Mater. Chem. A*, 2011, **21**, 13268.

30 C. X. Liu, R. Li, W. J. Liu, G. Z. Shen and D. Chen, Chitosan-assisted fabrication of a network C@V_2O_5 cathode for high-performance Zn-ion batteries, *ACS Appl. Mater. Interfaces*, 2021, **13**, 37194–37200.

31 Y. X. Zeng, Z. Z. Lai, Y. H. Han, H. Z. Zhang, S. L. Xie and X. H. Lu, Oxygen-vacancy and surface modulation of

ultrathin nickel cobaltite nanosheets as a high-energy cathode for advanced Zn-ion batteries, *Adv. Mater.*, 2018, **33**, 1802396.

32 J. Zhang, C. Q. Dong, Z. B. Wang, H. Gao, J. Z. Niu, Z. Q. Peng and Z. H. Zhang, A new defect-rich CoGa layered double hydroxide as efficient and stable oxygen evolution electrocatalyst, *Small Methods*, 2019, **3**, 1800286.

33 Y. Liu, P. Hu, H. Liu, X. Wu and C. Zhi, Tetragonal VO_2 hollow nanospheres as robust cathode material for aqueous zinc ion batteries, *Mater. Today Energy*, 2020, **17**, 100431.

34 X. Y. Chen, L. B. Wang, H. Li, F. Y. Cheng and J. Chen, Porous V_2O_5 nanofibers as cathode materials for rechargeable aqueous zinc-ion batteries, *J. Energy Chem.*, 2019, **38**, 20–25.

35 S. Y. Deng, H. Li, B. H. Chen, Z. J. Xu, Y. Jiang, C. H. Li, W. Xiao and X. M. Yan, High performance of Mn-doped VO_2 cathode for aqueous zinc-ion batteries: an insight into Zn^{2+} storage mechanism, *Chem. Eng. J.*, 2023, **452**, 139115.

36 J. W. Li, K. McColl, X. K. Lu, S. Sathasivam, H. B. Dong, L. Q. Kang, Z. N. Li, S. Y. Zhao, A. G. Kafizas, R. Wang, D. J. L. Brett, P. R. Shearing, F. Cora, G. J. He, C. J. Carmalt and I. P. Parkin, Multi-Scale investigations of δ-$Ni_{0.25}V_2O_5{\cdot}nH_2O$ cathode materials in aqueous zinc-ion batteries, *Adv. Energy Mater.*, 2020, **10**, 2000058.

37 D. D. Jia, K. Zheng, M. Song, H. Tan, A. Zhang, L. H. Wang, L. J. Yue, D. Li, C. W. Li and J. Q. Liu, $VO_2{\cdot}0.2H_2O$ nanocuboids anchored onto graphene sheets as the cathode material for ultrahigh capacity aqueous zinc ion batteries, *Nano Res.*, 2020, **13**, 215–224.

38 W. J. Li, C. Han, Q. F. Gu, S. L. Chou, J. Z. Wang, H. K. Liu and S. X. Dou, Electron delocalization and dissolution-restraint in vanadium oxide superlattices to boost electrochemical performance of aqueous zinc-ion batteries, *Adv. Energy Mater.*, 2020, **10**, 2001852.

39 N. Qiu, Z. M. Yang, R. Xue, Y. Wang, Y. M. Zhu and W. Liu, Toward a high-performance aqueous zinc ion battery: potassium vanadate nanobelts and carbon enhanced zinc foil, *Nano Lett.*, 2021, **21**, 2738–2744.

40 X. Wang, B. J. Xi, X. J. Ma, Z. Y. Feng, Y. X. Jia, J. K. Feng, Y. T. Qian and S. L. Xiong, Boosting zinc-ion storage capability by effectively suppressing vanadium dissolution based on robust layered barium vanadate, *Nano Lett.*, 2020, **20**, 2899–2906.

41 H. G. Qin, L. L. Chen, L. M. Wang, X. Chen and Z. H. Yang, V_2O_5 hollow spheres as high rate and long life cathode for aqueous rechargeable zinc ion batteries, *Electrochim. Acta*, 2019, **306**, 307–316.

42 H. F. Liang, Z. Cao, F. W. Ming, W. L. Zhang, D. H. Anjum, Y. Cui, L. Cavallo and H. N. Alshareef, Aqueous zinc-ion storage in MoS_2 by tuning the intercalation energy, *Nano Lett.*, 2019, **19**, 3199–3206.

43 Z. Y. Feng, Y. F. Zhang, J. J. Sun, Y. Y. Liu, H. M. Jiang, M. Cui, T. Hu and C. G. Meng, Dual ions enable vanadium oxide hydration with superior Zn^{2+} storage for aqueous zinc-ion batteries, *Chem. Eng. J.*, 2022, **433**, 133795.